**Research Article**

# Enhanced electromagnetic wave absorption property of binary ZnO/NiCo$_2$O$_4$ composites

Bin DU[*], Mei CAI, Xuan WANG, Junjie QIAN, Chao HE, Anze SHUI

*School of Materials Science and Engineering, South China University of Technology, Guangzhou 510641, China*

© The Author(s) 2021.

**Abstract:** Nowadays, metal oxide-based electromagnetic wave absorbing materials have aroused widely attentions in the application of telecommunication and electronics due to their selectable mechanical and outstanding dielectric properties. Herein, the binary ZnO/NiCo$_2$O$_4$ nanoparticles were successfully synthesized via hydrothermal reaction and the electromagnetic wave absorption properties of the composites were investigated in detail. As a result, benefiting from the dielectric loss, the as-obtained ZnO/NiCo$_2$O$_4$-7 samples possessed a minimum reflection loss value of –33.49 dB at 18.0 GHz with the thickness of 4.99 mm. This work indicates that ZnO/NiCo$_2$O$_4$ composites have the promising candidate applications in electromagnetic wave absorption materials in the future.

**Keywords:** ZnO particles; dielectric loss; magnetic loss; electromagnetic wave absorption

## 1 Introduction

In recent years, due to the rapid applications of electronic devices, electromagnetic wave pollution, considered as the fourth pollution source, has aroused widely attentions in the scientific community [1–6]. This is because electromagnetic wave not only threats information security but also the health of human beings [7–9]. In the past few years, numerous effects have been conducted to weaken or eliminate this pollution [10–15]. To date, electromagnetic wave absorbing materials are considered as the most popular strategies due to the various candidate materials with their low reflection [16–18]. Generally, the efficiency of electromagnetic wave absorbing performance is highly dependent on the electromagnetic wave absorption materials, including structures and components

[19,20]. Until now, numerous electromagnetic wave absorbing materials, including carbon [21–24], ceramics [25–28], conductive polymers [29], metal oxides [30–33], and magnetic metals [34–39], have been investigated and applied in real. Although those single-component materials have been widely studied in the past few years, constructing the composites with unique structures to improve the electromagnetic wave absorption properties via synergistic effects is still a mainstream trend.

Among various composites, metal oxide semiconductor-based materials are considered as the most promising candidates due to their unique electronic property, diverse forms, and tailored dielectric and magnetic loss. Liu *et al.* [40] synthesized a CoNi@SiO$_2$@TiO$_2$ microsphere. The results demonstrated that as-obtained samples exhibited remarkable microwave absorption properties with the reflection loss of –58.2 dB at 10.4 GHz with the thickness of 2.1 mm. However, the fabrication process is rather complex. Wang *et al.* [41] also reported a flexible broadband CC@ZnO electromagnetic wave

* Corresponding author.
E-mail: dubin@scut.edu.cn

absorbing material. Benefiting from high concentration of polarized charge, multiple reflection, and orientation polarization, the CC@ZnO composites exhibited excellent electromagnetic wave absorption performance with reflection loss reaching –43.6 dB with the thickness of 2.0 mm. Zhou *et al.* [34] synthesized a hierarchical CoNi@SiO$_2$@C composite through adjusting the dose of phenolic resin and achieved remarkable and broad bandwidth absorbing capability at the thickness only 2.2 mm. This advanced work also involved complication process and it is difficult to achieve amount of the samples. Recent advances in the preparation of hybrid electromagnetic wave absorbing materials clearly demonstrate that rational design microstructure is also critical in determining absorption properties. NiCo$_2$O$_4$ is considered as a good electromagnetic wave absorbing material for its high dielectric loss [42–45]. For example, Zhou *et al.* [44] revealed that the NiCo$_2$O$_4$ nano-flakes possess a minimum reflection loss of –25.5 dB at 4.5 GHz. However, such nano-flakes possessed weak electromagnetic wave absorbing performance. After synthesizing hierarchical core–shell C@NiCo$_2$O$_4$@Fe$_3$O$_4$ composites [46], the samples exhibited significant enhancement electromagnetic wave absorbing properties and the reflection loss increased to –43.0 dB at 13.4 GHz. Recently, Chang *et al.* [47] reported the different morphologies of NiCo$_2$O$_4$ particles as well as the electromagnetic wave absorbing performances. The results suggested that as-fabricated samples showed the large effective absorption bandwidth of 5.81 GHz. In addition, this work fabricated different morphologies of NiCo$_2$O$_4$ via adjusting the agent for the first time. Although numerous works have been conducted to fabricate NiCo$_2$O$_4$-based electromagnetic wave absorbing materials, most of them still restrict by its complex process. Thus, it remains a challenge to develop NiCo$_2$O$_4$-based electromagnetic wave absorbing materials with hybrid structure in a simple way.

In previous works, ZnO nanoparticles had been successfully fabricated by a simple method and the as-synthesized samples showed good electromagnetic wave absorbing performance [48]. In this work, a hybrid structure with binary ZnO/NiCo$_2$O$_4$ nanoparticles synthesized through hydrothermal reaction using nitrate and ammonium hydroxide and then the as-obtained powders were heated at 300 ℃. This simple method provides a new strategy to obtain the binary ZnO/NiCo$_2$O$_4$ composites with excellent electromagnetic wave absorption performance.

## 2 Experimental

### 2.1 Materials

Zinc nitrate (Zn(NO$_3$)$_2$·6H$_2$O), cobalt nitrate (Co(NO$_3$)$_2$·6H$_2$O), nickel nitrate (Ni(NO$_3$)$_2$·6H$_2$O), and ammonia aqueous solution (NH$_3$·H$_2$O, 25–30 wt%) were of analytical grade without further purification and purchased from Shanghai Aladdin Biochemical Technology Co., Ltd., China.

### 2.2 Synthesis of ZnO/NiCo$_2$O$_4$ nanoparticles

The ZnO/NiCo$_2$O$_4$ nanoparticles were fabricated by a facile hydrothermal reaction strategy. Typically, 0.30 g of Zn(NO$_3$)$_2$·6H$_2$O, 0.29 g of Ni(NO$_3$)$_2$·6H$_2$O, and 1.16 g of Co(NO$_3$)$_2$·6H$_2$O were gradually dissolved in deionized water (40 mL) using magnetic stirring. Then, different amounts of NH$_3$·H$_2$O (0.5, 0.7, and 1.0 mL) were added into the mixture solution and the color of mixture solution changed from milk white to baby blue. The corresponded specimens were labeled as ZnO/NiCo$_2$O$_4$-5, ZnO/NiCo$_2$O$_4$-7, and ZnO/NiCo$_2$O$_4$-10, respectively. Subsequently, the solution was transformed into a Teflon reactor and carried out at 200 ℃ for 18 h. The resulting black particles were washed by ethanol and distilled water for several times. Finally, the obtained brown powders were treated at 300 ℃ at air atmosphere for 2 h to obtain ZnO/NiCo$_2$O$_4$ nanoparticles.
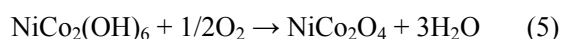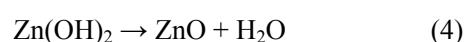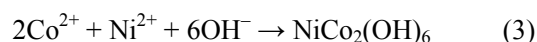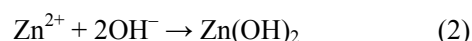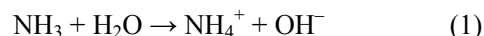
### 2.3 Characterization

The phase structure was characterized by X-ray diffraction (XRD) using a Rigaku D/max-3C equipped with Cu Kα radiation source ($\lambda = 0.1541$ nm) operating at 40 kV. The morphologies and microstructures were analyzed by a field-emission scanning electron microscope (FE-SEM, Helions Nanolab600i, USA) and a transmission electron microscope (TEM, CM300, Philips, the Netherlands), respectively. The magnetic characters of the as-prepared samples were observed via a vibrating sample magnetometer (VSM, Lakeshore 7407, USA) at room temperature. The specific surface and pore size distribution were analyzed by nitrogen adsorption–desorption isotherms (ASAP2020, USA). To evaluate the electromagnetic parameters, a vector network analyzer (Agilent Technologyies N5230A, USA) was utilized in 2.00–18.00 GHz. The powders were homogeneous mixed with paraffin at a mass ratio of 1:1 and then pressed into a circle shape ($\Phi_{outer} = 7.00$ mm, $\Phi_{inter} = 3.04$ mm) with the thickness of 2.5 mm. The reflection loss

values were calculated by the electromagnetic parameters according to the transmission line theory.

# 3 Results and discussion

The phase and crystal structure of the as-obtained powders are analyzed by XRD and the results are shown in Fig. 1(a). The peaks located at 32°, 34°, 36°, 52°, 47°, 57°, 59°, and 62° can be confirmed to hexagonal ZnO phase (PDF#99-0111). The remain peaks, including 31°, 33°, 37°, 38°, 39°, 44°, and 65° can be indexed to the $NiCo_2O_4$ phase (PDF#20-0781). The detailed formation of ZnO and $NiCo_2O_4$ phases can be described as followings: Firstly, the cationic of $Ni^{2+}$ and $Co^{2+}$ diffused around the $Zn(OH)_2$ particles, and formed the nucleus of $NiCo_2(OH)_6$ for the minimization of its surface energy according to Eqs. (1)–(3). Then, during the heat-treatment process, the $Zn(OH)_2$ and $NiCo_2(OH)_6$ hybrid particles converted into ZnO and $NiCo_2O_4$ hybird nanoparticles simultaneously according to Eqs. (4) and (5) [43–45,47], respectively. Meanwhile, no other peaks of the impurity are observed in XRD pattern, indicating that the high purity of the as-obtained powders. Figures 1(b)–1(d) demonstrate the morphologies of the as-obtained powders observed by SEM. As shown in Fig. 1, both the $ZnO/NiCo_2O_4$-5 and $ZnO/NiCo_2O_4$-7 samples are irregular shape particles ranging from several nanometers to hundred nanometers (Figs. 1(b) and 1(c)). The SEM image of $ZnO/NiCo_2O_4$-10 apparently represents a well-regulated structure (Fig. 1(d)). Amounts of well-regulated particles arrange together. The different morphologies of $ZnO/NiCo_2O_4$ nanoparticles are attributed to the concentration of the alkalinity. As reported in Ref. [45], with increasing the concentration of alkalinity, i.e., increasing the amount of $NH_3 \cdot H_2O$, the ZnO nanoparticles are easy to form the large-dimensional growth units and therefore, form the well-regulated particles.

$$NH_3 + H_2O \rightarrow NH_4^+ + OH^- \quad (1)$$

$$Zn^{2+} + 2OH^- \rightarrow Zn(OH)_2 \quad (2)$$

$$2Co^{2+} + Ni^{2+} + 6OH^- \rightarrow NiCo_2(OH)_6 \quad (3)$$

$$Zn(OH)_2 \rightarrow ZnO + H_2O \quad (4)$$

$$NiCo_2(OH)_6 + 1/2O_2 \rightarrow NiCo_2O_4 + 3H_2O \quad (5)$$

To further confirm the microstructure of the $ZnO/NiCo_2O_4$ nanoparticles, TEM was utilized and the results are shown in Fig. 2. From Fig. 2(a), it can be found that as-synthesized nanoparticles form an aggregate particle. As seen from Fig. 2(b), the lattice plane of the main phase is about 0.26 nm corresponding to (002) lattice type plane in hexagonal structure of ZnO (*P63mc*). In addition, the nano-dots can be identified as $NiCo_2O_4$ phase. The lattice space of the nano-dot is about 0.23 nm (Fig. 2(c)), consistent with the distance of (222) plane of the $NiCo_2O_4$. The surface-scanning element mapping (Fig. 2(d)) clearly demonstrates the distribution of elements. Obviously, the Zn elements distribute uniformly in the nanoparticle; whereas the Ni and Co elements show discontinuous distribution in the nanoparticle.
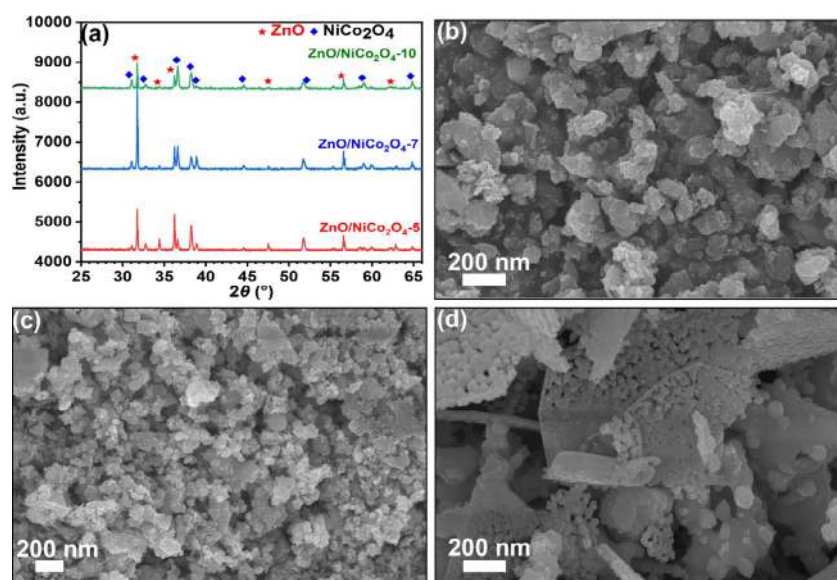


**Fig. 1** (a) XRD patterns and (b–d) SEM images of the as-obtained samples: (b) $ZnO/NiCo_2O_4$-5, (c) $ZnO/NiCo_2O_4$-7, and (d) $ZnO/NiCo_2O_4$-10.
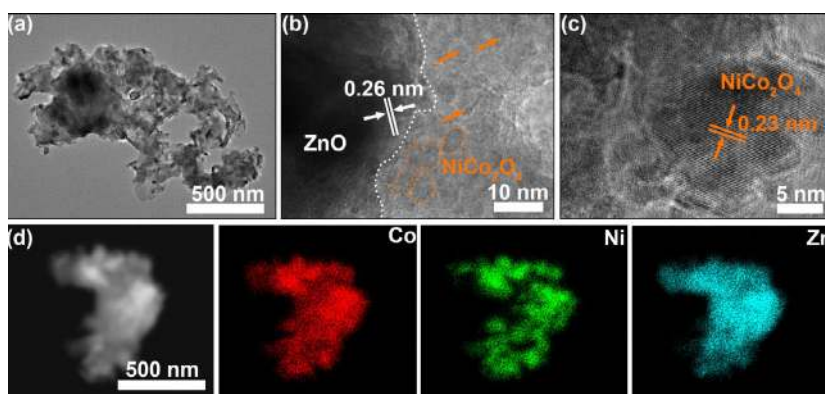
**Fig. 2**   TEM and high resolution TEM (HRTEM) images of the ZnO/NiCo$_2$O$_4$-7 nanoparticles: (a) TEM, (b, c) HRTEM, and (d) EDS mapping.

To confirm the porous attributes of the ZnO/NiCo$_2$O$_4$ nanoparticles, the nitrogen adsorption test was performed. The nitrogen adsorption–desorption isotherms and pore size distribution curves of all samples are shown in Fig. 3. It can be seen that as-obtained ZnO/NiCo$_2$O$_4$ samples represent type IV curves with a hysteresis loop (Fig. 3(a)), suggesting the existence of mesopores in the sample. Meanwhile, the Brunner−Emmet−Teller (BET) surface area of the ZnO/NiCo$_2$O$_4$-5, ZnO/NiCo$_2$O$_4$-7, and ZnO/NiCo$_2$O$_4$-10 samples are calculated to 86.85, 22.57, and 80.13 m$^2$/g, respectively. In addition, the pore size of the ZnO/NiCo$_2$O$_4$ sample mainly ranges in 0–40 nm calculated by the Barrett–Joyner–Halenda (BJH) method. Therefore, we can conclude that the as-obtained ZnO/NiCo$_2$O$_4$ sample contains mesopores and micropores, simultaneously.

Figure 4 shows the hysteresis loop of ZnO/NiCo$_2$O$_4$-7 nanoparticles at room temperature. The saturation magnetization (*Ms*) and the coercivity (*Hc*) of nanoparticle are 0.0007 emu/g and 60 Oe, respectively (Fig. 4(b)). The results clearly indicate that synthesized nanoparticles are nonmagnetic. This is mainly due to formation of nonmagnetic ZnO and NiCo$_2$O$_4$ phases. It is well known that ZnO is a multifunctional semiconductor and NiCo$_2$O$_4$
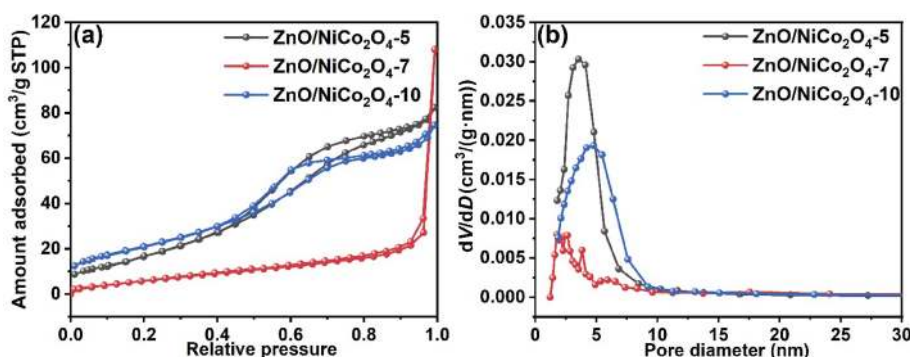


**Fig. 3**   (a) Nitrogen sorption isotherms of the samples and (b) BJH for the samples.
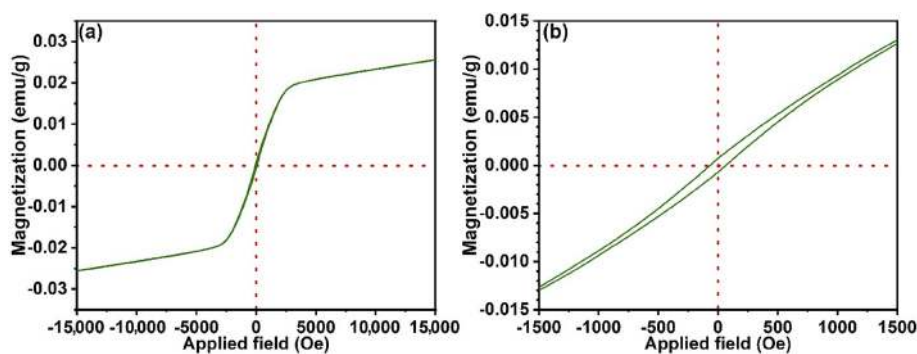


**Fig. 4**   (a) Hysteresis loop and (b) partly hysteresis loop for ZnO/NiCo$_2$O$_4$-7 nanoparticles.

is a nonmagnetic material at room temperature. Therefore, the as-synthesized ZnO/NiCo$_2$O$_4$-7 nanoparticles are nonmagnetic.

To evaluate the electromagnetic wave absorption performance of the binary ZnO/NiCo$_2$O$_4$ nanoparticles, complex permeability and permittivity of the as-synthesized samples were analyzed. Figure 5 demonstrates the dates for the as-obtained samples in the range of 2.0–18.0 GHz. From Figs. 5(a) and 5(b), it can be seen that both the real ($\varepsilon'$) and imaginary ($\varepsilon''$) parts of the permittivity increase with increasing the NH$_3$·H$_2$O content. The maximum values of $\varepsilon'$ reach 5.78, 6.85, and 6.96 for the samples of ZnO/NiCo$_2$O$_4$-5, ZnO/NiCo$_2$O$_4$-7, and ZnO/NiCo$_2$O$_4$-10, respectively. Meanwhile, the maximum values of $\varepsilon''$ increase to 0.39, 0.50, and 0.67 for the samples of ZnO/NiCo$_2$O$_4$-5, ZnO/NiCo$_2$O$_4$-7, and ZnO/NiCo$_2$O$_4$-10, respectively. It is generally accepted that the $\varepsilon'$ represents the storage energy ability via polarization; whereas $\varepsilon''$ shows the loss of energy by relaxation. Obviously, increasing the NH$_3$·H$_2$O content is good for increasing both real ($\varepsilon'$) and imaginary ($\varepsilon''$) parts of the permittivity, which means both the storage energy ability and transformation electromagnetic energy to heat energy are improved. Figure 5(c) represents the dielectric loss tangent ($\varepsilon''/\varepsilon'$) of the synthesized samples. It is clear that the values of $\varepsilon''/\varepsilon'$ also increase with increasing the NH$_3$·H$_2$O content and reach 0.068, 0.074, and 0.097

for the samples of ZnO/NiCo$_2$O$_4$-5, ZnO/NiCo$_2$O$_4$-7, and ZnO/NiCo$_2$O$_4$-10, respectively. In addition, the values of $\varepsilon''/\varepsilon'$ also increase with increasing frequency, indicating that dielectric loss mechanism enhanced with increasing frequency.

Figures 5(d) and 5(e) show the real ($\mu'$) and imaginary parts ($\mu''$) of complex permeability of the ZnO/NiCo$_2$O$_4$ samples. Compared with complex permittivity of the synthesized samples, both $\mu'$ and $\mu''$ show a sharp decrease with increasing frequency. Generally, $\mu'$ and $\mu''$ stand for the storage magnetic energy ability and magnetic loss energy, respectively. Herein, compared with other magnetic materials [14,15,20], ZnO/NiCo$_2$O$_4$ samples have the low values of $\mu'$. Thus, the stored magnetic energy ability of the ZnO/NiCo$_2$O$_4$ samples can be neglected. As shown in Figs. 5(e) and 5(f), some resonance peaks are found for the three samples. It is generally accepted that such resonance is attributed to the natural resonance, exchange resonance, and eddy current effect. According to Ref. [38], the exchange resonance usually was produced at high frequencies. Thus, we can infer that the fluctuates at low frequencies (4.0–8.0 GHz) and at high frequencies (12.0–18.0 GHz) should be associated with natural resonance and exchange resonance, respectively. In addition, the NiCo$_2$O$_4$ particles are in single domain range and therefore domain-wall displacement has a little effect on the magnetic energy loss [42].
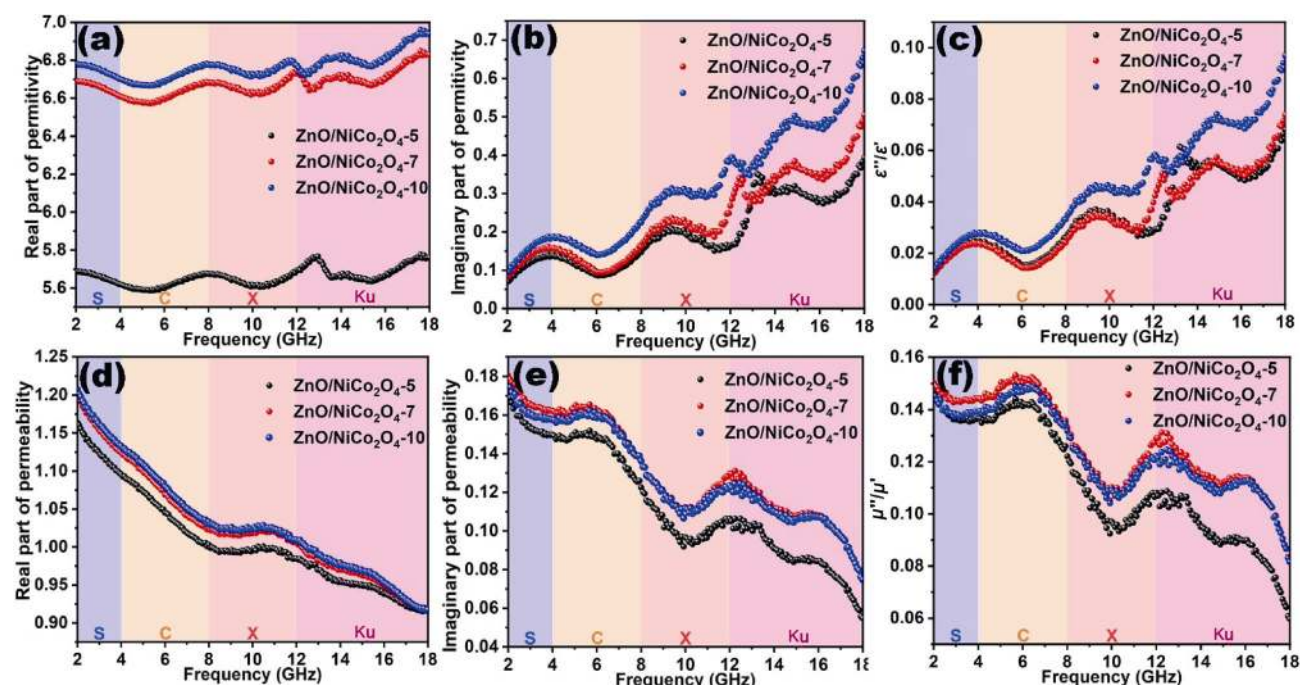


**Fig. 5** Electromagnetic parameters of the ZnO/NiCo$_2$O$_4$ range of 2.0–18.0 GHz: (a) real parts of permittivity ($\varepsilon'$); (b) imaginary parts of permittivity ($\varepsilon''$); (c) $\varepsilon''/\varepsilon'$; (d) real parts of permeability ($\mu'$); (e) imaginary parts of permeability ($\mu''$); and (f) $\mu''/\mu'$.

Since the magnetic hysteresis, ferromagnetic resonance, and domain-wall displacement has a little effect on the magnetic energy loss, the eddy current also needs to be investigated. Usually, the $C_0$ curve $C_0 = \mu''(\mu')^{-2}f^{-1}$, where $f$ stands for the frequency of electromagnetic wave, is used to evaluate the eddy current effect and the results are shown in Fig. 6. Generally, if the eddy current effect had contribution to the magnetic loss, the values of $C_0$ are constant when increasing the frequency. As it can be seen from Fig. 6(a), the $C_0$ values of the ZnO/NiCo$_2$O$_4$ samples gradually decrease within the frequency range of 2.0–18.0 GHz, suggesting that eddy current effect has no contribution for the magnetic energy loss in this range. Based on the above analysis, it can conclude that magnetic loss has a little effect on the electromagnetic wave absorbing performance.

According to the Debye dipolar relaxation theory, the complex form of real parts and imaginary parts of permittivity can be described as followings [49–52]:

$$[\varepsilon' - (\varepsilon_s + \varepsilon_\infty)/2]^2 + (\varepsilon'')^2 = [(\varepsilon_s - \varepsilon_\infty)/2]^2 \tag{6}$$

where $\varepsilon_s$ represents the stationary frequency dielectric constant and $\varepsilon_\infty$ stands for the infinite frequency dielectric constant. Theoretically considering that the plot of $\varepsilon''$ versus $\varepsilon'$ is a single semicircle according to Eq. (6). In fact, the plots show three parts of semicircles for all ZnO/NiCo$_2$O$_4$ samples (Fig. 6(b)), indicating the coexistence of multiple polarization processes, suggesting the enhanced Debye polarization process produced by multiple structures. When an alternation field applies on the samples, the charges will redistribute alternatively between ZnO particles and NiCo$_2$O$_4$ nano-dots. Thus, in addition to the dielectric loss of ZnO particles, the interfacial relaxation between ZnO and NiCo$_2$O$_4$ nano-dots also produces.

In recent years, the impedance matching degree ($\Delta$), which is the characteristic impedance of the sample between the free spaces, is used to elucidate the microwave absorbing capabilities in depth. The $\Delta$ can be described as following [53–55]:

$$|\Delta| = \left|\sinh^2(Kfd) - M\right| \tag{7}$$

$$K = \frac{4\pi\sqrt{\varepsilon'\mu'\sin\dfrac{\delta_\varepsilon + \delta_\mu}{2}}}{c\cos\delta_\varepsilon\cos\delta_\mu} \tag{8}$$

$$M = \frac{4\mu'\varepsilon'\cos\delta_\varepsilon\cos\delta_\mu}{\left(\mu'\cos\delta_\varepsilon - \varepsilon'\cos\delta_\mu\right) + \left[\tan\left(\dfrac{\delta_\mu}{2} - \dfrac{\delta_\varepsilon}{2}\right)\right]^2\left(\mu'\cos\delta_\varepsilon + \varepsilon'\cos\delta_\mu\right)^2} \tag{9}$$

where $d$ stands for the thickness of the sample; $c$ is the velocity of light in vacuum; $\delta_\varepsilon$ and $\delta_\mu$ are the dielectric loss angle and magnetic loss angle, respectively. Generally, the ideal value of $\Delta$ defined at 0.4 ($|\Delta| < 0.4$) [56,57]. It can be seen from Figs. 7(a)–7(c) that all the samples have the terrible values of $\Delta$ in the frequency range of S, C, and X bands. When increasing the thicknesses of ZnO/NiCo$_2$O$_4$-7 and ZnO/NiCo$_2$O$_4$-10 samples, the values of $\Delta$ gradually possess a little matching region at Ku band, suggesting that the as-synthesized samples may possess excellent electromagnetic wave absorption properties only in Ku band and a thickness more than 3.00 mm. However, the ZnO/NiCo$_2$O$_4$-5 samples still suffer a terrible matching region. Apart from the $\Delta$, the attenuation constant ($\alpha$) is another essential factor in determining the electromagnetic absorbing properties. The $\alpha$ usually represents the ability of dissipating the incident electromagnetic wave via dielectric and magnetic loss and can be described as following [58,59]:

$$\alpha = \frac{\sqrt{2}\pi f}{c} \times \sqrt{(\mu''\varepsilon'' - \mu'\varepsilon') + \sqrt{(\mu''\varepsilon'' - \mu'\varepsilon')^2 + (\mu''\varepsilon'' + \mu'\varepsilon')^2}} \tag{10}$$
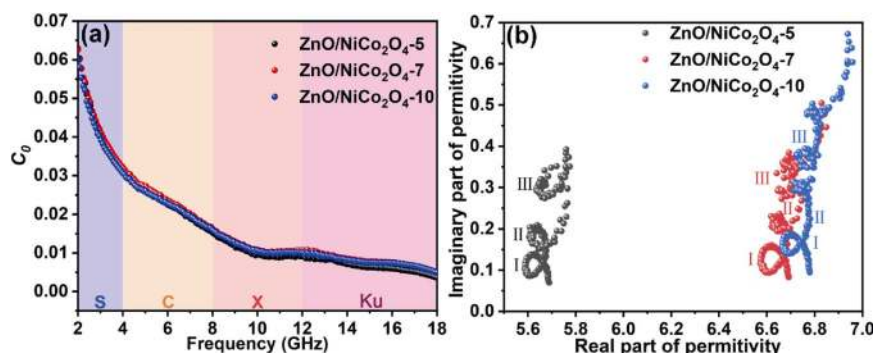
It can be seen from Fig. 7(d) that $\alpha$ values of the



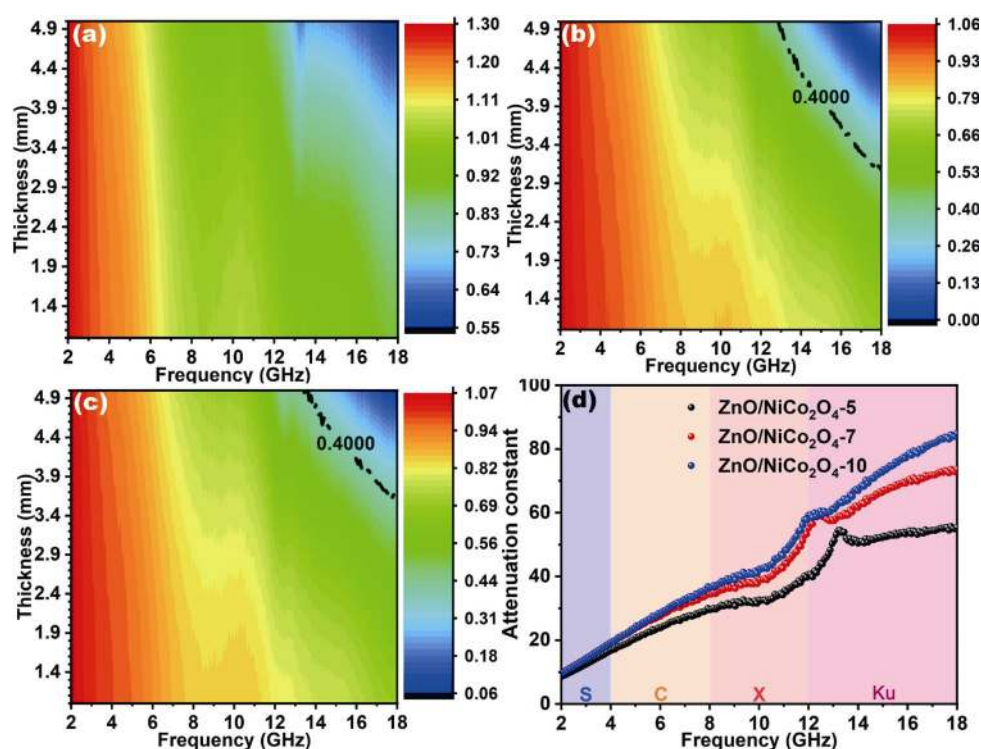**Fig. 6** (a) $C_0$ values and (b) Cole–Cole plots for the ZnO/NiCo$_2$O$_4$ samples.

**Fig. 7** (a–c) Color maps of the $\Delta$: (a) ZnO/NiCo$_2$O$_4$-5; (b) ZnO/NiCo$_2$O$_4$-7; (c) ZnO/NiCo$_2$O$_4$-10; and (d) $\alpha$ values of ZnO/NiCo$_2$O$_4$ samples.

ZnO/NiCo$_2$O$_4$ samples increase in the frequency range of 2.0–18.0 GHz. The detailed $\alpha$ values for ZnO/NiCo$_2$O$_4$-5, ZnO/NiCo$_2$O$_4$-7, and ZnO/NiCo$_2$O$_4$-10 are 55.65, 73.64, and 84.85, respectively. It is worth noting that $\alpha$ values are in good consistence with the complex permittivity and permeability parameters (Fig. 5). Therefore, it concluded that the synthesized ZnO/NiCo$_2$O$_4$ samples only possess excellent electromagnetic wave absorbing capabilities in high frequencies (> 16 GHz) when both the $\alpha$ and $\Delta$ are taken into consideration.

The electromagnetic wave absorbing properties of the synthesized samples are evaluated by their reflection loss (*RL*). According to transmission line theory, *RL* values can be calculated by the following equations [60–64]:

$$RL = 20\log\left|\frac{Z_{in}-1}{Z_{in}+1}\right| \qquad (11)$$

$$Z_{in} = \sqrt{\frac{\mu_r}{\varepsilon_r}}\tanh\left[j\left(\frac{2\pi}{c}\right)fd\sqrt{\mu_r\varepsilon_r}\right] \qquad (12)$$

Figure 8 displays the color maps for the *RL* of ZnO/NiCo$_2$O$_4$ in the frequency range of 2.0–18.0 GHz as well as the typical *RL* curves at a certain thickness. Clearly, all the samples possess poor electromagnetic wave absorption performance at the frequency below

~16.0 GHz. The results are in good consistence with the electromagnetic parameters, $\alpha$ and $\Delta$. Among those samples, ZnO/NiCo$_2$O$_4$-7 exhibits an excellent electromagnetic wave absorption performance, and its minimum *RL* value even increases to –33.49 dB at 18.0 GHz with the thickness of 4.99 mm (Fig. 8(b)). ZnO/NiCo$_2$O$_4$-10 shows inferior reflection loss intensities, and the minimum *RL* value is –27.46 dB at 17.92 GHz with the thickness of 4.99 mm (Fig. 8(d)). However, the ZnO/NiCo$_2$O$_4$-5 shows poor electromagnetic wave absorption properties and the minimum *RL* values only reaches –6.52 dB at 18.0 GHz with the thickness of 5.0 mm (Fig. 8(f)). Usually, incident electromagnetic wave is considered as –10.0 dB (means 90.0% of absorption efficiency). In this regard, the ZnO/NiCo$_2$O$_4$-5 is not an electromagnetic wave absorption material due to the gap between relative complex permittivity and permeability resulting in mismatched impedance. However, when increasing the NH$_3$·H$_2$O content, the numbers of ZnO and NiCo$_2$O$_4$ nanoparticles are enhanced, leading to increase the dielectric loss and interfacial relaxation. Table 1 represents the electromagnetic wave absorbing performance of the related materials. As observed from Table 1, ZnO/NiCo$_2$O$_4$-7 and ZnO/NiCo$_2$O$_4$-10 indeed display their promising candidates, the electromagnetic wave absorption materials at high frequencies.
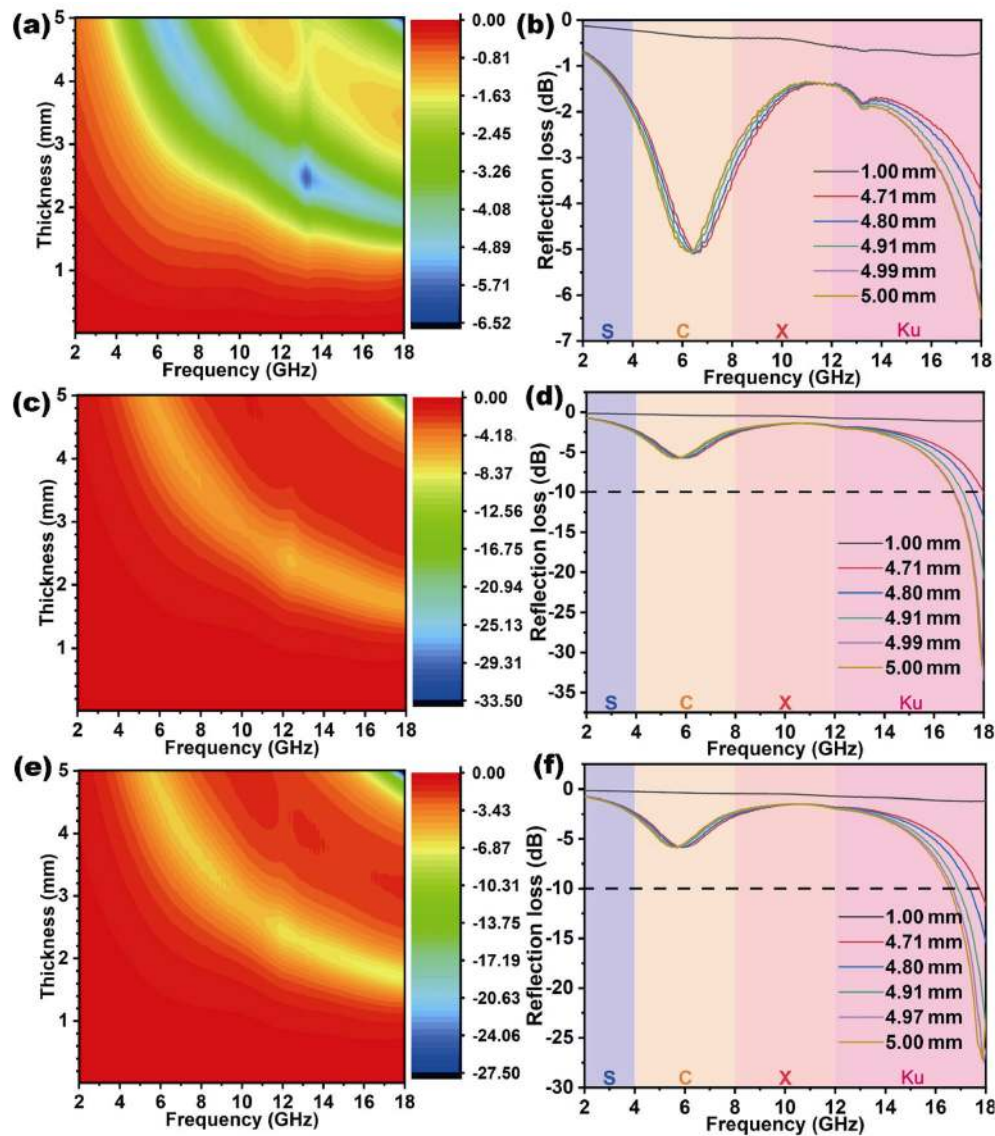
**Fig. 8** (a–f) Color maps of the reflection loss: (a, b) ZnO/NiCo$_2$O$_4$-5; (c, d) ZnO/NiCo$_2$O$_4$-7; and (e, f) ZnO/NiCo$_2$O$_4$-10.

**Table 1** Electromagnetic wave absorbing performance of the related materials reported in recent years

| Absorber | Minimum *RL* (dB) | Matching thickness (mm) | *f* (GHz) | Ref. |
|---|---|---|---|---|
| C@Fe$_3$O$_4$ | −45 | 3.4 | 6.18 | [17] |
| Co/C-700 | −15.7 | 1.7 | 15.1 | [20] |
| C/CoFe$_2$O$_4$ | −49.6 | 2.5 | 9.2 | [21] |
| C–SiOC | −27.6 | 1.5 | 13.8 | [26] |
| ZnO | −37.7 | 2.1 | 8.96 | [48] |
| ZnO/NiCo$_2$O$_4$ | −33.49 | 4.99 | 18.0 | This work |

## 4 Conclusions

In summary, the ZnO/NiCo$_2$O$_4$ hybrid nanoparticles were successfully synthesized by the hydrothermal reaction method. The increase of NH$_3$·H$_2$O content could increase the relative complex permittivity, visibly enhancing the dielectric loss of the samples. In addition, the unique structure and interfacial relaxation played a critical role on the dissipation of electromagnetic waves. The results also demonstrated that impedance matching degree and attenuation constant improved with increasing the content of NH$_3$·H$_2$O at high frequencies. Benefiting from the hybrid structure and components, the as-synthesized ZnO/NiCo$_2$O$_4$-7 sample possessed an excellent *RL* value of −33.49 dB at 18.0 GHz with the thickness of 4.99 mm. This result suggested that ZnO/NiCo$_2$O$_4$ was a promising candidate in microwave absorption applications in the future.

## Acknowledgements

## References

[1] Xu Z, Du YC, Liu DW, *et al*. Pea-like Fe/Fe$_3$C nanoparticles embedded in nitrogen-doped carbon nanotubes with tunable dielectric/magnetic loss and efficient electromagnetic absorption. *ACS Appl Mater Interfaces* 2019, **11**: 4268–4277.

[2] Chaudhary A, Kumari S, Kumar R, *et al*. Lightweight and easily foldable MCMB–MWCNTs composite paper with exceptional electromagnetic interference shielding. *ACS Appl Mater Interfaces* 2016, **8**: 10600–10608.

[3] Cao MS, Han C, Wang XX, *et al*. Graphene nanohybrids: Excellent electromagnetic properties for the absorbing and shielding of electromagnetic waves. *J Mater Chem C* 2018, **6**: 4586–4602.

[4] Wang Y, Du YC, Qiang R, *et al*. Interfacially engineered sandwich-like rGO/carbon microspheres/rGO composite as an efficient and durable microwave absorber. *Adv Mater Interfaces* 2016, **3**: 1500684.

[5] Eddib AA, Chung DDL. The importance of the electrical contact between specimen and testing fixture in evaluating the electromagnetic interference shielding effectiveness of carbon materials. *Carbon* 2017, **117**: 427–436.

[6] Balci O, Polat EO, Kakenov N, *et al*. Graphene-enabled electrically switchable radar-absorbing surfaces. *Nat Commun* 2015, **6**: 1–10.

[7] Liu Y, Chen Z, Xie WH, *et al*. *In-situ* growth and graphitization synthesis of porous Fe$_3$O$_4$/carbon fiber composites derived from biomass as lightweight microwave absorber. *ACS Sustain Chem Eng* 2019, **7**: 5318–5328.

[8] Shahzad F, Alhabeb M, Hatter CB, *et al*. Electromagnetic interference shielding with 2D transition metal carbides (MXenes). *Science* 2016, **353**: 1137–1140.

[9] Wang CX, Wang BB, Cao X, *et al*. 3D flower-like Co-based oxide composites with excellent wideband electromagnetic microwave absorption. *Compos B: Eng* 2021, **205**: 108529.

[10] Hou TQ, Jia ZR, Feng AL, *et al*. Hierarchical composite of biomass derived magnetic carbon framework and phytic acid doped polyanilne with prominent electromagnetic wave absorption capacity. *J Mater Sci Technol* 2021, **68**: 61–69.

[11] Wen B, Cao MS, Lu MM, *et al*. Reduced graphene oxides: Light-weight and high-efficiency electromagnetic interference shielding at elevated temperatures. *Adv Mater* 2014, **26**: 3484–3489.

[12] Wang GZ, Gao Z, Tang SW, *et al*. Microwave absorption properties of carbon nanocoils coated with highly controlled magnetic materials by atomic layer deposition. *ACS Nano* 2012, **6**: 11009–11017.

[13] Du Y, Liu W, Qiang R, *et al*. Shell thickness-dependent microwave absorption of core–shell Fe$_3$O$_4$@C composites. *ACS Appl Mater Interfaces* 2014, **6**: 12997–13006.

[14] Cheng Y, Cao JM, Li Y, *et al*. The outside-in approach to construct Fe$_3$O$_4$ nanocrystals/mesoporous carbon hollow spheres core–shell hybrids toward microwave absorption. *ACS Sustain Chem Eng* 2018, **6**: 1427–1435.

[15] Shi ZJ, Xing L, Liu Y, *et al*. A porous biomass-based sandwich-structured Co$_3$O$_4$@carbon fiber@Co$_3$O$_4$ composite for high-performance supercapacitors. *Carbon* 2018, **128**: 819–825.

[16] Zhang XJ, Zhu JQ, Yin PG, *et al*. Tunable high-performance microwave absorption of Co$_{1-x}$S hollow spheres constructed by nanosheets within ultralow filler loading. *Adv Funct Mater* 2018, **28**: 1800761.

[17] Meng FB, Wei W, Chen XN, *et al*. Design of porous C@Fe$_3$O$_4$ hybrid nanotubes with excellent microwave absorption. *Phys Chem Chem Phys* 2016, **18**: 2510–2516.

[18] Wang X, Pan F, Xiang Z, *et al*. Magnetic vortex core-shell Fe$_3$O$_4$@C nanorings with enhanced microwave absorption performance. *Carbon* 2020, **157**: 130–139.

[19] Liu DW, Du YC, Wang FY, *et al*. MOFs-derived multi-chamber carbon microspheres with enhanced microwave absorption. *Carbon* 2020, **157**: 478–485.

[20] Zhu BY, Miao P, Kong J, *et al*. Co/C composite derived from a newly constructed metal-organic framework for effective microwave absorption. *Cryst Growth Des* 2019, **19**: 1518–1524.

[21] Huang L, Li JJ, Wang ZJ, *et al*. Microwave absorption enhancement of porous C@CoFe$_2$O$_4$ nanocomposites derived from eggshell membrane. *Carbon* 2019, **143**: 507–516.

[22] Quan L, Qin FX, Estevez D, *et al*. Magnetic graphene for microwave absorbing application: Towards the lightest graphene-based absorber. *Carbon* 2017, **125**: 630–639.

[23] Zhao HB, Cheng JB, Zhu JY, *et al*. Ultralight CoNi/rGO aerogels toward excellent microwave absorption at ultrathin thickness. *J Mater Chem C* 2019, **7**: 441–448.

[24] Zhang F, Cui W, Wang BB, *et al*. Morphology-control synthesis of polyaniline decorative porous carbon with remarkable electromagnetic wave absorption capabilities. *Compos B: Eng* 2021, **204**: 108491.

[25] Du B, Qian JJ, Hu P, *et al*. Fabrication of C-doped SiC nanocomposites with tailoring dielectric properties for the enhanced electromagnetic wave absorption. *Carbon* 2020, **157**: 788–795.

[26] Du B, He C, Qian JJ, *et al*. Electromagnetic wave absorbing properties of glucose-derived carbon-rich SiOC ceramics annealed at different temperatures. *J Am Ceram Soc* 2019, **102**: 7015–7025.

[27] Luo CJ, Jiao T, Gu JW, *et al*. Graphene shield by SiBCN ceramic: A promising high-temperature electromagnetic wave-absorbing material with oxidation resistance. *ACS Appl Mater Interfaces* 2018, **10**: 39307–39318.

[28] Yu ZJ, Lv X, Mao KW, *et al*. Role of *in situ* formed free

carbon on electromagnetic absorption properties of polymer-derived SiC ceramics. *J Adv Ceram* 2020, **9**: 617–628.

[29] Gopakumar DA, Pai AR, Pottathara YB, *et al*. Cellulose nanofiber-based polyaniline flexible papers as sustainable microwave absorbers in the X-band. *ACS Appl Mater Interfaces* 2018, **10**: 20032–20043.

[30] Mo ZC, Yang RL, Lu DW, *et al*. Lightweight, three-dimensional carbon Nanotube@TiO₂ sponge with enhanced microwave absorption performance. *Carbon* 2019, **144**: 433–439.

[31] Han MK, Yin XW, Kong L, *et al*. Graphene-wrapped ZnO hollow spheres with enhanced electromagnetic wave absorption properties. *J Mater Chem A* 2014, **2**: 16403–16409.

[32] Dong S, Lyu Y, Li XT, *et al*. Construction of MnO nanoparticles anchored on SiC whiskers for superior electromagnetic wave absorption. *J Colloid Interface Sci* 2020, **559**: 186–196.

[33] Wang JW, Wang BB, Wang Z, *et al*. Synthesis of 3D flower-like ZnO/ZnCo₂O₄ composites with the heterogeneous interface for excellent electromagnetic wave absorption properties. *J Colloid Interface Sci* 2021, **586**: 479–490.

[34] Zhou SH, Huang Y, Liu XD, *et al*. Synthesis and microwave absorption enhancement of CoNi@SiO₂@C hierarchical structures. *Ind Eng Chem Res* 2018, **57**: 5507–5516.

[35] Gholampoor M, Movassagh-Alanagh F, Salimkhani H. Fabrication of nano-Fe₃O₄ 3D structure on carbon fibers as a microwave absorber and EMI shielding composite by modified EPD method. *Solid State Sci* 2017, **64**: 51–61.

[36] Liu T, Pang Y, Zhu M, *et al*. Microporous Co@CoO nanoparticles with superior microwave absorption properties. *Nanoscale* 2014, **6**: 2447–2454.

[37] Zhao ZH, Zhou XJ, Kou KC, *et al*. PVP-assisted transformation of ZIF-67 into cobalt layered double hydroxide/carbon fiber as electromagnetic wave absorber. *Carbon* 2021, **173**: 80–90.

[38] Zhao ZH, Kou KC, Wu HJ. 2-Methylimidazole-mediated hierarchical Co₃O₄/N-doped carbon/short-carbon-fiber composite as high-performance electromagnetic wave absorber. *J Colloid Interface Sci* 2020, **574**: 1–10.

[39] Zhang HX, Shi C, Jia ZR, *et al*. FeNi nanoparticles embedded reduced graphene/nitrogen-doped carbon composites towards the ultra-wideband electromagnetic wave absorption. *J Colloid Interface Sci* 2021, **584**: 382–394.

[40] Liu QH, Cao Q, Bi H, *et al*. CoNi@SiO₂@TiO₂ and CoNi@Air@TiO₂ microspheres with strong wideband microwave absorption. *Adv Mater* 2016, **28**: 486–490.

[41] Wang L, Li X, Li QQ, *et al*. Oriented polarization tuning broadband absorption from flexible hierarchical ZnO arrays vertically supported on carbon cloth. *Small* 2019, **15**: 1900900.

[42] Anu Prathap MU, Srivastava R. Electrochemical reduction of lindane (γ-HCH) at NiCo₂O₄ modified electrode. *Electrochimica Acta* 2013, **108**: 145–152.

[43] Zhang GQ, Lou XWD. General solution growth of mesoporous NiCo₂O₄Nanosheets on various conductive

substrates as high-performance electrodes for supercapacitors. *Adv Mater* 2013, **25**: 976–979.

[44] Zhou M, Lu F, Chen B, *et al*. Thickness dependent complex permittivity and microwave absorption of NiCo₂O₄ nanoflakes. *Mater Lett* 2015, **159**: 498–501.

[45] Fu HH, Liu Y, Chen L, *et al*. Designed formation of NiCo₂O₄ with different morphologies self-assembled from nanoparticles for asymmetric supercapacitors and electrocatalysts for oxygen evolution reaction. *Electrochim Acta* 2019, **296**: 719–729.

[46] Wei S, Wang XX, Zhang BQ, *et al*. Preparation of hierarchical core–shell C@NiCo₂O₄@Fe₃O₄ composites for enhanced microwave absorption performance. *Chem Eng J* 2017, **314**: 477–487.

[47] Chang Q, Liang HS, Shi B, *et al*. Ethylenediamine-assisted hydrothermal synthesis of NiCo₂O₄ absorber with controlled morphology and excellent absorbing performance. *J Colloid Interface Sci* 2021, **588**: 336–345.

[48] Cai M, Shui AZ, Wang X, *et al*. A facile fabrication and high-performance electromagnetic microwave absorption of ZnO nanoparticles. *J Alloys Compd* 2020, **842**: 155638.

[49] Zhao B, Deng JS, Zhang R, *et al*. Recent advances on the electromagnetic wave absorption properties of Ni based materials. *Eng Sci* 2018, **3**: 5–40.

[50] Cao MS, Yang J, Song WL, *et al*. Ferroferric oxide/multiwalled carbon nanotube vs polyaniline/ferroferric oxide/multiwalled carbon nanotube multiheterostructures for highly effective microwave absorption. *ACS Appl Mater Interfaces* 2012, **4**: 6949–6956.

[51] Cao MS, Wang XX, Cao WQ, *et al*. Thermally driven transport and relaxation switching self-powered electromagnetic energy conversion. *Small* 2018, **14**: 1800987.

[52] Cao MS, Wang XX, Zhang M, *et al*. Variable-temperature electron transport and dipole polarization turning flexible multifunctional microsensor beyond electrical and optical energy. *Adv Mater* 2020, **32**: 1907156.

[53] Zhao B, Guo XQ, Zhao WY, *et al*. Facile synthesis of yolk-shell Ni@void@SnO₂(Ni₃Sn₂) ternary composites via galvanic replacement/Kirkendall effect and their enhanced microwave absorption properties. *Nano Res* 2017, **10**: 331–343.

[54] Wang YH, Han XJ, Xu P, *et al*. Synthesis of pomegranate-like Mo₂C@C nanospheres for highly efficient microwave absorption. *Chem Eng J* 2019, **372**: 312–320.

[55] Meng F, Wei W, Chen X, *et al*. Design of porous C@Fe₃O₄ hybrid nanotubes with excellent microwave absorption. *Phys Chem Chem Phys* 2016, **18**: 2510–2516.

[56] Wang YH, Li CL, Han XJ, *et al*. Ultrasmall Mo2C nanoparticle-decorated carbon polyhedrons for enhanced microwave absorption. *ACS Appl Nano Mater* 2018, **1**: 5366–5376.

[57] Wang YH, Han XJ, Xu P, *et al*. Synthesis of pomegranate-like Mo2C@C nanospheres for highly efficient microwave absorption. *Chem Eng J* 2019, **372**: 312–320.

[58] Liu PB, Zhu CY, Gao S, *et al*. N-doped porous carbon

nanoplates embedded with $CoS_2$ vertically anchored on carbon cloths for flexible and ultrahigh microwave absorption. *Carbon* 2020, **163**: 348–359.

[59] Liu PB, Gao S, Liu XD, *et al*. Rational construction of hierarchical hollow $CuS@CoS_2$ nanoboxes with heterogeneous interfaces for high-efficiency microwave absorption materials. *Compos B*: *Eng* 2020, **192**: 107992.

[60] Wang H, Wu LN, Jiao JF, *et al*. Covalent interaction enhanced electromagnetic wave absorption in SiC/Co hybrid nanowires. *J Mater Chem A* 2015, **3**: 6517–6525.

[61] Zhang N, Huang Y, Wang MY. 3D ferromagnetic graphene nanocomposites with ZnO nanorods and $Fe_3O_4$ nanoparticles co-decorated for efficient electromagnetic wave absorption. *Compos B*: *Eng* 2018, **136**: 135–142.

[62] Liu XF, Hao CC, Jiang H, *et al*. Hierarchical $NiCo_2O_4/$$Co_3O_4/NiO$ porous composite: A lightweight electromagnetic wave absorber with tunable absorbing performance. *J Mater Chem C* 2017, **5**: 3770–3778.

[63] Shu RW, Li WJ, Wu Y, *et al*. Fabrication of nitrogen-doped cobalt oxide/cobalt/carbon nanocomposites derived from heterobimetallic zeolitic imidazolate frameworks with superior microwave absorption properties. *Compos B*: *Eng*

2019, **178**: 107518.

[64] Bora PJ, Azeem I, Vinoy KJ, *et al*. Morphology controllable microwave absorption property of polyvinylbutyral (PVB)-$MnO_2$ nanocomposites. *Compos B*: *Eng* 2018, **132**: 188–196.